

Strongly coupled redox-linked conformational switching at the active site of the non-heme iron-dependent dioxygenase, TauD

Christopher W. John,¹ Greg M. Swain,¹ Robert P. Hausinger,^{2,3} and Denis A. Proshlyakov¹

1 Department of Chemistry, Michigan State University, East Lansing, MI 48824, USA

2 Department of Microbiology and Molecular Genetics, Michigan State University, East Lansing, MI 48824, USA

3 Department of Biochemistry and Molecular Biology, Michigan State University, East Lansing, MI 48824, USA

ABSTRACT: 2-Oxoglutarate (2OG)-dependent dioxygenases catalyze C-H activation while performing a wide range of chemical transformations. In contrast to their heme analogues, non-heme iron centers afford greater structural flexibility with important implications for their diverse catalytic mechanisms. We characterize an *in situ* structural model of the putative transient ferric intermediate of 2OG:taurine dioxygenase (TauD) by using a combination of spectroelectrochemical and semi-empirical computational methods, demonstrating that the Fe (III/II) transition involves a substantial, fully reversible, redox-linked conformational change at the active site. This rearrangement alters the apparent redox potential of the active site between -127 mV for reduction of the ferric state and 171 mV for oxidation of the ferrous state of the 2OG-Fe-TauD complex. Structural perturbations exhibit limited sensitivity to mediator concentrations and potential pulse duration. Similar changes were observed in the Fe-TauD and taurine-2OG-Fe-TauD complexes, thus attributing the reorganization to the protein moiety rather than the cosubstrates. Redox difference infrared spectra indicate a reorganization of the protein backbone in addition to the involvement of carboxylate and histidine ligands. Quantitative modeling of the transient redox response using two alternative reaction schemes across a variety of experimental conditions strongly supports the proposal for intrinsic protein reorganization as the origin of the experimental observations.

INTRODUCTION

The 2-oxoglutarate (2OG)-dependent dioxygenases activate C-H bonds while catalyzing a variety of biologically relevant reactions,¹ including synthesis of a wide range of commercial products.² 2OG:taurine dioxygenase (TauD), the archetypical member of this enzyme family,^{3,4} is found in *Escherichia coli* where it metabolizes taurine (2-aminoethane sulfonate) as a sulfur source for sulfur-starved cells.⁵ TauD activates taurine via hydrogen atom transfer (HAT) to an Fe(IV)=O intermediate J (shown as F4 in Fig.1),⁶ followed by hydroxyl rebound and product degradation.⁷

A time-resolved resonance Raman study of TauD revealed the existence of two transient intermediates that trailed F4 in time and assigned them to the $\nu_{\text{Fe-O}}$ and ν_{as} modes of the ferric (hydr)oxo (F3) and alkoxo (FX) intermediates, respectively.⁸ HAT by F4 in TauD is analogous to HAT by Compound I in cytochromes P450 (CYP450)⁹ except that TauD is expected to yield a transient non-heme Fe(III)-OH complex (Fig. 1) instead of a heme Fe(IV)-OH in Compound II of CYP450. However, the Raman study found no vibrational evidence for protonation of the oxo group in F3, attributing its absence to a proton transfer to a nearby base that allows for the formation of an ensuing FX species. While the alkoxo structure of FX received additional support in a recent crystallographic study of another 2OG-dependent hydroxylase, VioC,¹⁰ the lack of proton sensitivity of F3 is unexpected for two reasons. First, the Raman study⁸ was conducted at pH 8 and well below the $\text{p}K_{\text{a}} \approx 25$ (in DMSO) reported for Fe(III)-OH model complexes.¹¹ The low dielectric environment of the active site¹² is also expected to increase the $\text{p}K_{\text{a}}$ over that in an aqueous medium. Second, the $\text{p}K_{\text{a}}$ of F3 contributes to the HAT capacity of F4 per Bordwell's thermodynamic cycle (Fig. 1),^{13,14} as has been demonstrated for the analogous $\text{p}K_{\text{a}}$ of Compound II in CYP450 ($\text{p}K_{\text{a}} = 12$)¹⁵ in contrast to peroxidases ($\text{p}K_{\text{a}} < 4$).^{16,17} Since the geometry of the Fe(III)-OH ligand may reduce the sensitivity of the $\nu_{\text{Fe-OH}}$ Raman mode to $^1\text{H}/^2\text{H}$ substitution, it is important to examine the protonation state of F3 using other techniques.

Spectroelectrochemistry can reveal protonation events either directly from spectroscopic changes or indirectly from the pH sensitivity of the Fe(II)/Fe(III) redox potential.^{3,18,19} This information can then be used to reconstruct the protonation states of Fe(III)-TauD as an *in situ* model of the transient F3 species from the known crystallographic structures of Fe(II)-TauD. The weak UV-Vis absorption of the non-heme iron center in TauD²⁰ makes direct detection of the Fe(II)/Fe(III) redox transition by optical spectroscopy impractical. Much of the pioneering work

by Mäntele *et al.*^{21–23} focused on proteins with porphyrin cofactors, with their strong, oxidation state-sensitive optical absorption spectra. Similar methods were applied to the relatively intense chromophores in copper enzymes^{18,24} and Ni-Fe hydrogenases.^{25,26} As an alternative to optical spectroscopy, one can exploit reaction-induced infrared (IR) difference spectroscopy^{27,28} for the detection of reversible vibrational changes of ligands in response to the redox state changes of the metal.^{29,30} Here, we investigated several complexes of TauD (Fig. 1) using normal pulse spectrovoltametry (NPSV) with IR detection to identify structural and redox properties simultaneously.³¹ This study revealed a redox-linked conformational change at the active site of TauD that modulates its redox potential at an unprecedented magnitude.

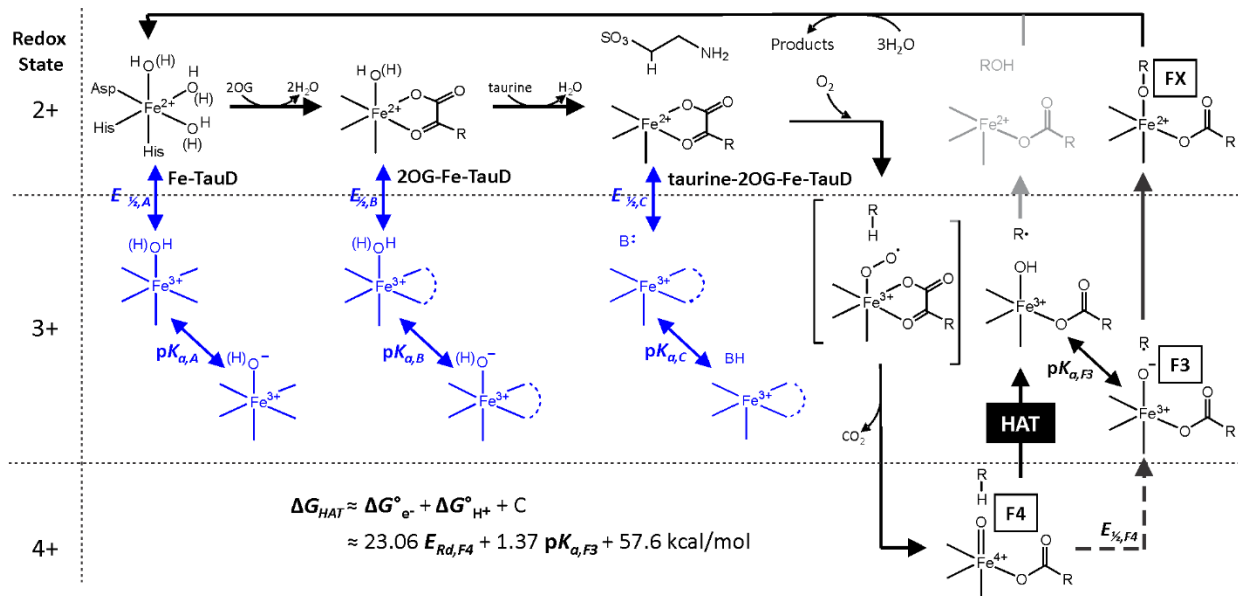


Figure 1. Redox states of catalytic intermediates and artificial complexes of TauD. Vertical transitions indicate a change in the oxidation state of the Fe center. Diagonal transitions indicate a change in a protonation state. Grey structures show the classical hydroxyl radical rebound pathway. Blue structures illustrate electrochemical manipulation of TauD to model the F3 state.

METHODS

Sample preparation

TauD apoprotein was purified as previously described³² with the following modifications: cell cultures were grown in six 2 L flasks, each containing 1 L of Terrific Broth medium, at 37 °C and with shaking at 200 rpm. A final concentration of 1 mM isopropyl β-D-1-thiogalactopyranoside was added to each flask after reaching an O.D. of 0.6 at 600 nm. The

temperature was reduced to 30 °C and the cultures were grown overnight. Pelleted cells were stored at -80 °C until needed. The cells were thawed and resuspended in a lysis buffer containing 20 mM Tris, pH 8, 1 mM ethylenediaminetetraacetic acid, and 1 mM phenylmethanesulfonyl fluoride prior to being lysed by sonication.

Fe(III)-TauD was prepared by adding a 1:1 molar ratio of ferrous ammonium sulfate to TauD apoprotein under anaerobic conditions, followed by oxidation using a 5-fold excess of ferricyanide (FCN) for 1 h and the removal of ferri/ferrocyanide using a GE Healthcare PD-10 desalting column. Fe(III)-TauD samples were stored on ice in 25 mM Tris buffer, pH 8.

The final sample buffer was exchanged using a 10 kDa centrifugation membrane unit (Amicon). 2OG-Fe(III)-TauD and taurine-2OG-Fe(III)-TauD were prepared by adding 2-fold excess of 2OG and/or 3-fold excess of taurine to approximately 1 mM Fe(III)-TauD. FCN, methylene green (MG), and thionine acetate (TA) mediators were added to achieve 100 μ M of each in the final solution, unless noted otherwise. All samples were prepared in 25 mM Tris buffer at pH 8.5 in D₂O with 0.5 M KCl.

Spectroscopic measurements

NPSV measurements were performed using a 12.5 μ m pathlength optically transparent thin layer electrochemical (OTTLE) cell³¹ over a boron-doped diamond working electrode and a Ag/AgCl (0.5 M KCl) reference electrode at 10 °C.^{33,34} Electrochemical measurements were performed using a computer-controlled potentiostat (Model CHI1202b, CH Instruments). Reference potentials (E_r) in reduction and oxidation modes were +0.5 V and -0.6 V, respectively, with a potential increment of 0.04 V. The potential pulse duration was 300 s, unless otherwise noted, with FTIR spectra acquisition (Equinox 55/S, Bruker) during the final 120 s (Fig. S1). NPSV data were analyzed by a non-linear global spectral regression (GSR)³⁵ and kinetic simulations were performed using KinESim³⁶ packages for Igor Pro.³¹

The solution rate constants k_{sol} for the reaction of MG and TA with Fe(III)-TauD were determined as previously described for myoglobin (Mb).³¹ The k_{sol} for the oxidation of Fe(II)-TauD by FCN was determined anaerobically while stirring against 100 μ M FCN in 25 mM Tris buffer, pH 8. The reaction was initiated by the injection of Fe(II)-TauD to achieve an equimolar ratio with the mediator. UV-Vis spectra (Hewlett Packard 8453) were collected every 2 s for 20 s

before and 10 min after the start of the reaction. The bimolecular rate constant was obtained by fitting the temporal changes at 420 nm.

RESULTS

NPSV (Fig. S1) utilizes a series of applied potentials, $E_{a,i}$, each incremented by a defined potential step and preceded by a reference potential, $E_{r,i}$. The absolute Fourier transform infrared (FTIR) spectra were acquired at the end of each potential step over a spectral integration period when the reaction had reached equilibrium. Spectra acquired sequentially under alternating potentials $E_{a,i}$ ($S_{a,i}$) and $E_{r,i}$ ($S_{r,i}$) formed a raw absolute data matrix (Fig. S2, top). This matrix was reduced into a redox difference matrix of spectra (ΔS_i , Fig. S2, bottom):

$$\Delta S_i = S_{a,i} - \frac{1}{2} (S_{r,i} + S_{r,(i+1)}) \quad (1)$$

Experimental values of ΔS_i at 1681 cm^{-1} are shown by markers in Fig. 2, right. For the oxidation NPSV segment (blue) ΔA_{1681} was measured *vs.* $E_{r,i} = -0.6 \text{ V}$ as $E_{a,i}$ was increased from -0.14 to 0.34 V. For the reduction sweep (red), $E_{a,i}$ was decreased from 0.14 to -0.38 V and ΔA_{1681} was measured *vs.* $E_{r,i} = +0.5 \text{ V}$.

The redox-difference dataset (ΔS) was deconvoluted into a full occupancy spectra, ΔS_{tot} , and Nernstian population profiles, ϕ , so that each redox difference spectrum ΔS_i at the i -th NPSV step is described as:

$$\Delta S_i = \Delta S_{\text{tot}} \times \phi_i \quad (2)$$

where $\phi_i = f(E_{a,i}, E_{1/2}, n)$ is a property of the analyte and the applied potential (E_a).³¹ The resulting profiles ϕ (lines in Fig. 2, right) represent E_a -dependent intensities of the entire spectra ΔS_{tot} (Fig. 2, left) as opposed to experimental ΔA at a selected frequency (markers).

Fe-TauD is redox inactive on the electrode without mediators (MG, TA, and FCN), each of which is also described by its own ΔS_{tot} , $E_{1/2}$, and n .³¹ Fig. 2 shows ΔS_{tot} (left) and ϕ (right) of the Fe(II)/Fe(III) transition in 2OG-Fe-TauD, while Fig. S3 compares it with the same transition in Fe-TauD and taurine-2OG-Fe-TauD. Notably, mediators are described by their own matrices $\Delta S = \Delta S_{\text{tot}} \times \phi$ and do not contribute to TauD spectra.

The close similarities between the reduction and oxidation FTIR spectra in all three complexes show that the observed redox processes are fully reversible. The spectra were

dominated by vibrational changes in the 1550-1700 cm^{-1} region, outside of which only a vibration at $\sim 1400 \text{ cm}^{-1}$ was consistently observed in all forms. Redox changes in the 1650-1700 cm^{-1} region were specific to the 2OG-containing complexes and were altered upon taurine binding (Fig. S3). All complexes exhibited changes in the amide I stretching region at 1632/1624 cm^{-1} (Fe-TauD) or 1638/1630 cm^{-1} (2OG-Fe-TauD and taurine-2OG-Fe-TauD).³⁷ A prominent trough was observed at 1580 cm^{-1} in Fe-TauD with a likely corresponding peak at 1614 cm^{-1} ; these features showed a 20 cm^{-1} downshift upon binding of 2OG (2OG-Fe-TauD and taurine-2OG-TauD).

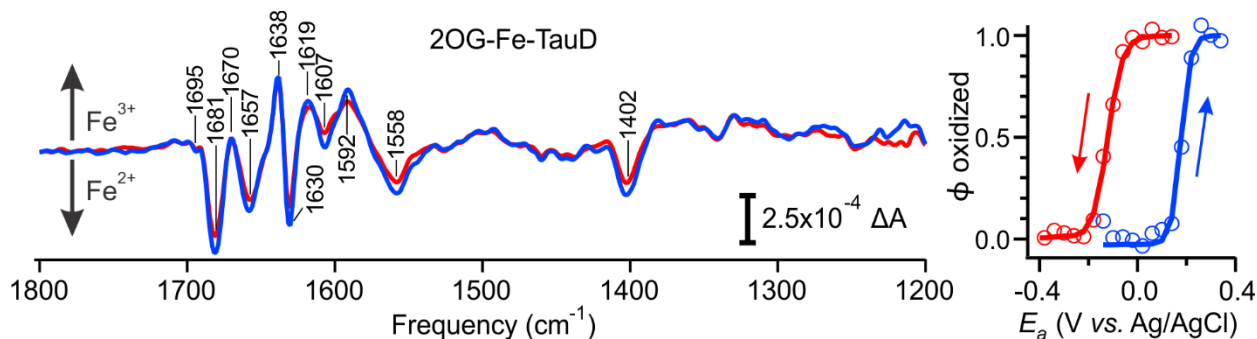


Figure 2. NPSV transitions in 2OG-Fe-TauD. Redox mediators: 100 μM MG, 100 μM TA, and 100 μM FCN. **Left:** $\Delta\text{S}_{\text{tot}}$ of reduction (red, vs. $E_r = 0.5\text{V}$) and oxidation (blue, vs. $E_r = -0.6\text{V}$) steps. **Right:** Experimental profiles of reduction steps (red circles) and oxidation steps (blue circles) normalized using ΔA_{1681} with ϕ_{rd} (red) and ϕ_{ox} (blue) profiles. For ease of comparison, both $\Delta\text{S}_{\text{tot}}$ and ϕ are shown as the Fe(III)/Fe(II) redox difference.

In contrast to the redox spectra, the reduction and oxidation population profiles, ϕ_{rd} and ϕ_{ox} , were sharply different, exhibiting a large separation of apparent potentials (Fig. 2, right) and the appearance of minor oxidation phases in Fe-TauD and taurine-2OG-Fe-TauD (Fig. S3). Results of fitting ϕ to Nernstian profiles with $n = 1$ are shown in Table S1. The appearance of a large redox hysteresis in all three forms of TauD contrasts with the behavior of Mb using the same OTTLE cell, electrode, and mediators (except FCN),³¹ raising the possibility that the shift in potentials originates from the difference in the specific interactions of reduced and oxidized forms of the mediator with the protein moiety rather than $E_{1/2}^A$ of the metal. This possibility was excluded using Zn^{2+} -substituted TauD,²⁰ which was found to be redox inactive (Fig. S4), attributing the observed changes to the redox transitions of the iron center.

The second possibility is that the apparent shift in potentials arises from the kinetic or thermodynamic limitations of the TauD/mediator reactions, particularly due to the redox gap between the $E_{1/2}$ of FCN and the other two mediators (Table S2), which is comparable in

magnitude to the hysteresis observed in TauD. Since this potential gap could not be bridged experimentally due to low solubility, instability, or irreversible interactions of other mediators with TauD (Table S3), the role of kinetic limitations of a discontinuous ladder of mediators was investigated using a semi-empirical model of heterogeneous mediated electrochemistry (Fig. S5).³¹ Since this model was developed using the same mediators and electrochemical system as reported here, it required only parametrization of FCN, including the mediator-specific heterogeneous potential-dependent (k_{et}^*) and potential-independent (k_{lim}) effective rate-limiting constants on the electrode and the bimolecular rate constant (k_{sol}) for the homogeneous FCN/TauD reaction (Table S2). These kinetic parameters were used to simulate concentration profiles of TauD, which were integrated over specified time periods to obtain ϕ and compared with experimental profiles obtained under identical conditions.

Two alternative reaction schemes were investigated to assess the origin of the redox hysteresis in TauD (Fig. 3). In the single state model [1], identical to what was used for Mb,³¹ TauD exists in a simple redox equilibrium with a single redox potential, $E_{1/2}^A$. The redox hysteresis using [1] could originate only from the inefficiency of the mediators. The redox-linked switching model [2] includes at least two distinct conformations of TauD, conformers A and A', each with a distinct redox potential (Fig. 3, right). Since the experimental NPSV data report the combined contribution of all isomers of TauD, simulated populations of conformers A and A' were combined as well. The combined populations yielded only one or two apparent NPSV transitions even if the responses of individual conformers were more complex. Conformational changes of TauD using [2] are described by separate sets of rates and equilibria constants in the reduced and oxidized states. The values of k_1 and k_2 were estimated from the slow phases of oxidation by FCN and were found to be approximately $9 \times 10^{-4} \text{ s}^{-1}$ (Fig. S6). The extent of the oxidation of Fe(II)-TauD by FCN over the first 30 s allowed for the estimation of $K_1 \geq 10^2$ and the reverse isomerization rate $k_{-1} \approx 10^{-5} \text{ s}^{-1}$. Since $\Delta G = 0$ for a cyclic process, one can calculate $K_2 = 9.6 \times 10^{-6}$ from experimental estimates of $E_{1/2}^A$, $E_{1/2}^{A'}$, and K_1 .

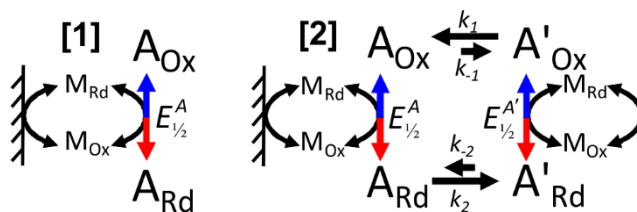


Figure 3. Chemical models for the mediated electrochemistry of TauD. The single state model [1] describes a homogeneous population of A, with a single redox potential, $E_{1/2}^A$. The redox switching model [2] allows for redox-linked isomerization of the analyte between conformations A and A' with distinct redox potentials, $E_{1/2}^A$ and $E_{1/2}^{A'}$, respectively, and preferential stability in the oxidized and reduced forms. Direct electron transfer is allowed only for the mediator M. See text for the estimates and interpretation of forward and reverse isomerization rates.

The NPSV response was predicted for the two alternative models for 2OG-Fe-TauD while varying $E_{1/2}^A$ (for [1]) or $E_{1/2}^A$ and $E_{1/2}^{A'}$ (for [2]). The simulated ϕ_{Ox}^A and ϕ_{Rd}^A profiles shown in Fig. 4 and Fig. S7 are directly comparable to those obtained from experimental NPSV data in Fig. 2, right. Simulations using [1] with an $E_{1/2}^A$ within 50 mV of that of any mediator show nearly complete reversibility, as was observed for Mb.³¹ As $E_{1/2}^A$ approached the middle of the potential gap between MG and FCN, ϕ^A exhibited an increasing degree of distortion with the

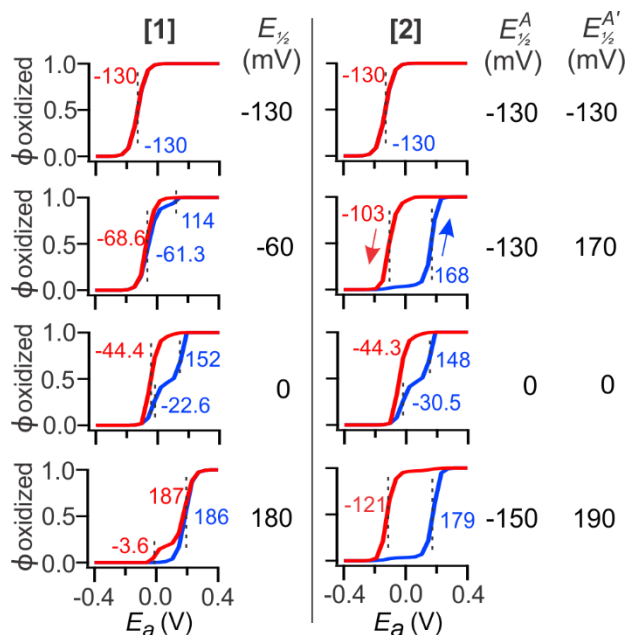


Figure 4. Effect of thermodynamic properties of the analyte on the apparent NPSV redox hysteresis for models [1] and [2]. Simulated ϕ_{Rd} (red) and ϕ_{Ox} (blue) profiles of an analyte (A) that is completely dependent on mediators (Table S2). The intrinsic $E_{1/2}$ of A (left) or A, A' (right) used in simulations are indicated to the right of each plot. The observed $E_{1/2}$ values are indicated next to each transition, including minor transitions, where present.

development of an apparent hysteresis between -60 and +140 mV in the reduction and oxidation modes, respectively, and the appearance of minor redox transitions (Fig. 5 and Table S4). At $E_{1/2}^A = 0$ mV the hysteresis reaches a maximum amplitude of 213 mV, which is much smaller than the 298 mV hysteresis observed in TauD. The largest hysteresis of 199 mV was observed using [1] with symmetrical ϕ_{Ox}^A and ϕ_{Rd}^A and $E_{1/2}^A = 60$ mV (Fig. S7).

Analogous simulations using model [2], with the addition of $E_{1/2}^{A'}$, confirmed that the profile of ϕ^{TauD} and the magnitude of the observed hysteresis depend primarily on the intrinsic potentials $E_{1/2}^A$ and $E_{1/2}^{A'}$ (Fig. 4) when their difference is large. When $E_{1/2}^A \approx E_{1/2}^{A'}$, [2] reduces to [1] and the observed ϕ^{TauD} was determined by the gap in the mediator ladder. Therefore, there were multiple conditions where the shape of ϕ^{TauD} alone was not sufficient to unambiguously distinguish between [1] and [2] based on the hysteresis alone. However, the two models predict different sensitivities to mediator concentrations, particularly that of FCN due to the absence other mediators in its effective potential range.

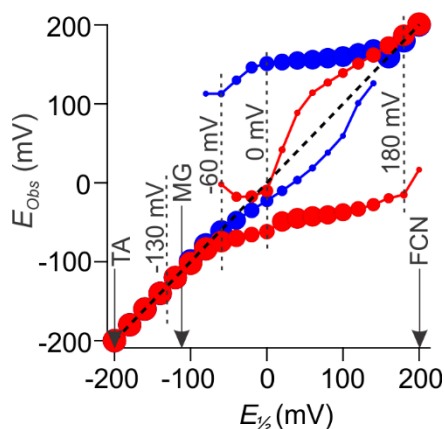


Figure 5. The effect of the intrinsic $E_{1/2}$ on NPSV redox transitions in model [1]. Simulations and NPSV integrations were performed under realistic conditions. Marker sizes represent relative amplitudes of the major and minor fitted phases (E_{Obs}) of corresponding ϕ^A profiles in the reduction (●) and oxidation (●) NPSV modes. The intrinsic $E_{1/2}^A$ illustrated in Fig. 4, left, are indicated by vertical dashed lines and their intercepts with the plot represent the apparent transitions. The diagonal dashed line represents ideal Nernstian behavior. Arrows indicate the $E_{1/2}$ of individual mediators.

The effects of FCN concentration on ϕ_{Ox} and ϕ_{Rd} using models [1] vs. [2] are illustrated in Fig. 6. For [1], we selected $E_{1/2} = 60$ mV for which the hysteresis is the most sensitive to FCN

concentration. Simulations using [2] were conducted with $E_{1/2}^A = -140$ mV and $E_{1/2}^{A'} = 100$ mV, as these values yielded an apparent hysteresis comparable to that observed experimentally. An increase in the concentration of FCN from 0.1 mM to 2.5 mM decreased the oxidation E_{Obs} by 66 mV using [1] (131 mV – 65.2 mV) and 78 mV using [2] (158 mV – 80 mV) vs. the experimentally observed decrease of 121 mV (171 mV – 50 mV). Oxidation E_{Obs} using [2] decreased below $E_{1/2}^{A'}$ in agreement with the continuous changes in experimental value (Fig. 6, middle) and contrary to the exponential saturation predicted for [1]. However, the largest discrepancy was observed in the apparent reduction potential, which increased using [1] and remained essentially unchanged using [2]. As a result, [1] predicts the loss of the hysteresis at 2.5 mM FCN, in contrast to the hysteresis of 198 mV observed experimentally and 184 mV predicted using [2]. The contribution of the minor phase also diminishes at high FCN concentration.

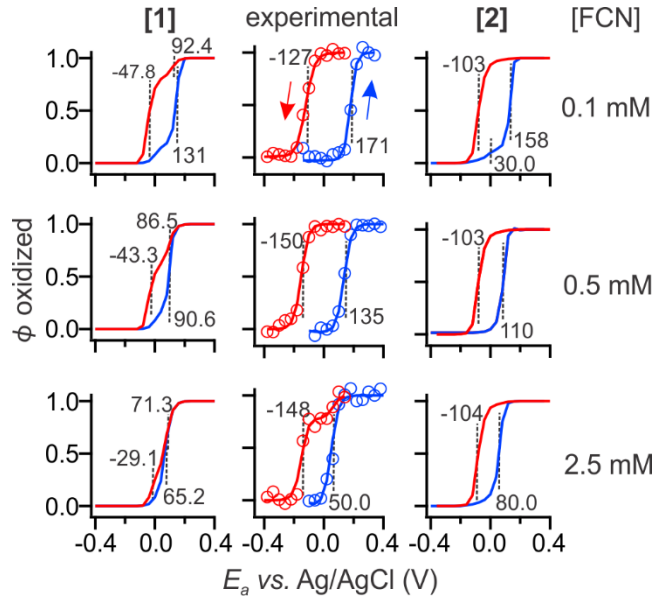


Figure 6. The effect of FCN concentration on the observed ϕ_{Rd} and ϕ_{Ox} profiles. Experimental ϕ_{Rd}^{TauD} (\circ) and ϕ_{Ox}^{TauD} (\circ) for 1 mM TauD (center) are compared with corresponding profiles predicted by models [1] (left) and [2] (right) at the indicated concentrations of FCN. The $E_{1/2}^A$ using [1] was 60 mV. $E_{1/2}^A$ and $E_{1/2}^{A'}$ using [2] were -130 and 100 mV, respectively. The E_{Obs} (mV) of major phases are shown.

The complete removal of FCN is expected to hinder the oxidation process and exacerbate the non-ideal behavior of TauD differently for models [1] and [2], allowing for further discrimination between the models. As the applied potentials $E_{a,4}$ and $E_{a,5}$ approach $E_{1/2}$ (Fig. 7,

left; NPV cycles 4 and 5), facile reduction of the analyte leads to large changes in its population during the $\bar{\phi}_{r,4} \rightarrow \bar{\phi}_{a,4}$ and $\bar{\phi}_{r,5} \rightarrow \bar{\phi}_{a,5}$ steps. This effect increases the reversible NPSV response using [1] ($\Delta\bar{\phi}_4$ and $\Delta\bar{\phi}_5$), which is defined as $\Delta\bar{\phi}_i = \bar{\phi}_{a,i} - 0.5(\bar{\phi}_{r,i} + \bar{\phi}_{a,i+1})$.³¹ However, this reduction is followed by only a minimal re-oxidation during $\bar{\phi}_{a,4} \rightarrow \bar{\phi}_{r,5}$ and $\bar{\phi}_{a,5} \rightarrow \bar{\phi}_{r,6}$ steps due to the limited oxidizing capacity of low potential mediators. Subsequent steps show exhaustive reduction with smaller amplitudes ($\bar{\phi}_{a,6}$) and the NPSV response of the mostly reduced sample falls ($\Delta\bar{\phi}_6$; Fig 7, right). This process results in a pseudo-equilibrium region where changes in $\bar{\phi}_i$ become potential-independent due to inefficient oxidation of TauD by MG and TA even at a high E_r (shaded area in Fig. 7). The magnitude of $\Delta\bar{\phi}$ in this region represents only the extent of the change in redox state ($\Delta\bar{\phi}_7 < 20\%$, right) and not the major redox state of TauD ($>80\%$ reduced $\bar{\phi}_{a,7}$ and $\bar{\phi}_{r,7}$, left).

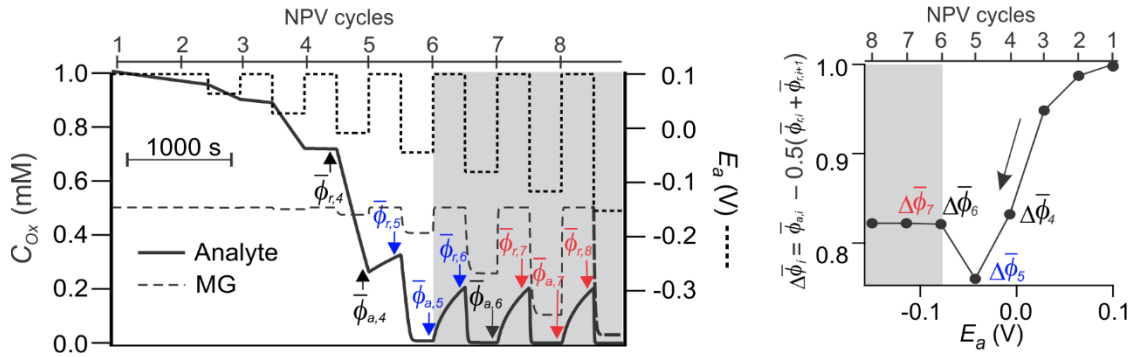


Figure 7. Kinetically limited NPSV reduction profile in the absence of FCN. *Left:* The concentration of oxidized analyte (solid line, $E_{1/2} = 80$ mV) and oxidized MG (dashed line) predicted by [1] over successive NPSV cycles (dotted line). Simulation conditions for a realistic mediator cocktail are identical to the 1000 s pulse width data in Fig. 8 (left). TA is present, but not shown for clarity. Integrated $\bar{\phi}_i$ that determine $\Delta\bar{\phi}_5$ and $\Delta\bar{\phi}_7$ are shown in blue and red, respectively. *Right:* The integrated NPSV profile for E_a decreasing from +0.1 V to -0.2 V over eight steps against $E_r = 0.1$ V. The maximal amplitude is observed for $\Delta\bar{\phi}_5$ due to facile reduction during the $\bar{\phi}_{r,5} \rightarrow \bar{\phi}_{a,5}$ step. The amplitudes of $\Delta\bar{\phi}_{\geq 6}$ are decreased due to the slow reduction, i.e. $\bar{\phi}_{a,7} \rightarrow \bar{\phi}_{r,8}$ step. An expanded view of this profile is shown in Fig. 8 (left top, open markers) in comparison with shorter pulse duration and the oxidation mode profiles. The pseudo-equilibrium region is highlighted in grey.

A different response can be expected using [2] in the absence of FCN, because protein isomerization provides an alternative pathway for oxidation of A' via A. Furthermore, both models predict that non-equilibrium ϕ profiles would exhibit substantial dependence on pulse duration and analyte potentials. Predictions of the two models (Fig. 8 left and right) differ in

three characteristic parameters. i) The onsets of the ϕ_{Ox} and ϕ_{Rd} transitions using [1] are narrow (up to $\Delta\bar{\phi}_5$ in Fig. 7) and follow the profiles of an $n = 1$ redox process. Using [1] this is followed by a sharp transition to the pseudo-equilibrium phase ($\Delta\bar{\phi}_6$ in Fig. 7). In contrast, the onset is much broader using [2] ($n = 0.2 - 0.5$, for the best fit lines in Fig. 8, right) and no distinct pseudo-equilibrium region is observed. ii) The alternative oxidation pathway using [2] results in a larger NPSV amplitude following the onset of the redox transition. A second NPSV peak in the reduction mode is predicted using [2] under some conditions (Fig. S8), which reflects a direct contribution of the low potential redox transition. The pseudo-equilibrium region using [1] is always featureless and its amplitude diminishes rapidly at high $E_{1/2}$. iii) The apparent potentials of maximal ϕ_{Ox} and ϕ_{Rd} responses are close to the intrinsic $E_{1/2}^A$ using [1] ($\Delta E_{Obs} = 110$ mV) in contrast to a much larger apparent difference for [2] ($\Delta E_{Obs} = 330$ mV) (Fig. 8, black lines). The experimental ϕ^{TauD} , obtained at 300 s and 1000 s NPSV pulse widths, are compared to the matching simulations using models [1] and [2] in Fig. 8 and S7. As argued above for Fig. 4, experimental observations for the full mediator cocktail limit $E_{1/2}^A$ using [1] to the range of 40 - 80 mV, but these $E_{1/2}^A$ values result in a substantially larger ϕ amplitude in the absence of FCN than observed experimentally (Fig. S8). The maximum experimental NPSV amplitude of 2OG-Fe-TauD with 300 s and 1000 s pulses in the absence of FCN (Fig. 8) was > 0.7 mM and < 0.18 mM for the reduction and oxidation modes, respectively. Such an amplitude was observed using [1] only for $E_{1/2}^A$ of +100 to +130 mV, where the hysteresis in the full mediator cocktail is already smaller than observed for TauD. The experimental NPSV onset was much broader than predicted for [1] with $E_{1/2} < +130$ mV and showed a better correlation using simulation [2] with $E_{1/2}^{A'} > +140$ mV. The relative amplitudes of ϕ_{Ox}^{TauD} and ϕ_{Rd}^{TauD} with 300 s or 1000 s NPV pulse widths further support model [2] over [1].

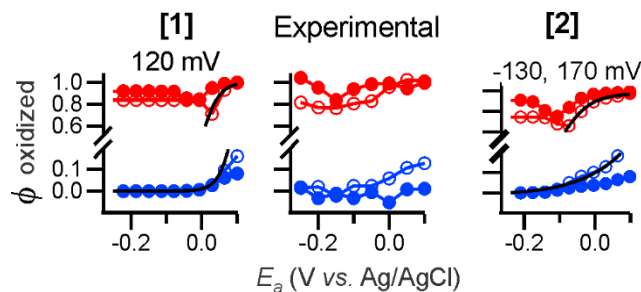


Figure 8. Comparison of experimental NPSV hysteresis with model-dependent predictions in the absence of FCN.

Experimental ϕ_{Rd}^{TauD} (●, ○) and ϕ_{Ox}^{TauD} (●, ○) of 1 mM TauD with 0.5 mM MG and saturated TA (<150 μ M) but no FCN (center) are compared with corresponding profiles predicted by models [1] (left) and [2] (right). The origin of the characteristic reduction response using [1] (top left) is illustrated in Fig. 7. Experimental and simulated profiles were acquired for 300 s (●, ●) and 1000 s (○, ○) NPSV pulse widths. Best fit Nernstian profiles are shown for reference (—; [1]: $n = 1$, $\Delta E_{obs} = 0.11$ V; [2]: $n_{ox} = 0.53$, $n_{rd} = 0.23$, $\Delta E_{obs} = 0.33$ V).

DISCUSSION

The redox cycle of anaerobic Fe-TauD is vibrationally fully reversible (Fig. 2). The observation of an electrochemical hysteresis in all forms of TauD (Fig. S3) was surprising and sharply contrasts with the simple redox transition of myoglobin.³¹ The lack of suitable mediators with $E_{1/2}$ of 0 – 100 mV required us to conduct an investigation into the role of kinetic and thermodynamic limitations of mediated electrochemistry using two alternative models (Fig. 3) before being able to state unequivocally that the hysteresis is attributed to intrinsic properties of Fe-TauD. The application of a semi-empirical model of heterogeneous thin layer electrochemistry showed that both models can yield comparable NPSV results using specific Fe-TauD potentials at the given mediator concentrations. However, no single $E_{1/2}^{TauD}$ value in model [1] could yield ϕ_{Ox} and ϕ_{Rd} consistent with experimental observations across all the conditions tested here, giving strong support for intrinsic redox-linked reorganization in Fe-TauD, as follows.

The largest hysteresis predicted for model [1] was 213 mV ($E_{1/2}^{TauD} = 0.0$ mV), which is 85 mV smaller than that experimentally observed in 2OG-Fe-TauD and taurine-2OG-Fe-TauD and 128 mV smaller than that observed in Fe-TauD (Table S1). The magnitude of the hysteresis and apparent $E_{1/2}^{TauD}$ values in 2OG-Fe-TauD and taurine-2OG-Fe-TauD could be reproduced by model [2] using $E_{1/2}^A = -130$ mV and $E_{1/2}^{A'} = 180$ mV (Fig. S7). The observed reduction $E_{1/2}^{TauD}$ are within the effective potential range of MG and TA, as is evident for Mb,³¹ and a negligible

hysteresis is predicted for [1] with $E_{1/2} = -130$ mV (Fig. 4). This observation is important for two reasons. First, if TauD has a single $E_{1/2}$ that falls within the effective range of TA and MG, both the reduction and oxidation should occur at this potential unless there is a major difference in the interaction of TauD with the reduced or oxidized forms of both MG and TA, which falls into the definition of [2]. Second, the $E_{1/2}$ of Mb (-157 mV by NPSV, no hysteresis) is similar to the observed reduction potential of Fe-TauD (-154 mV, large hysteresis).³¹ The differences in the bimolecular rates of electron transfer between the mediators and Mb or TauD are negligible for the NPSV pulse duration and an equilibrium is expected to be reached before each spectral acquisition.

The observed oxidation $E_{1/2}^{\text{TauD}}$ may be biased positive if it falls below the effective range for the current FCN concentration and well above the $E_{1/2}$ of MG. Such bias can be reduced or eliminated at higher FCN concentrations in both models in agreement with the observed $\phi_{\text{Ox}}^{\text{TauD}}$ (Fig. 6); however, the two models predicted an increasingly divergent response of the apparent reduction potential with increasing FCN. The observed $\phi_{\text{Rd}}^{\text{TauD}}$ showed distinctly better agreement with model [2] than with [1].

The complete removal of FCN as a mediator resulted in several characteristic features in the calculated $\phi_{\text{Rd}}^{\text{TauD}}$ and $\phi_{\text{Ox}}^{\text{TauD}}$ profiles that arise from the imbalance between the reduction and oxidation rates³¹ and could be used to further discriminate between models [1] and [2] (Fig. 8, Fig. S8). The redox transition using [1] starts with an escalating amplitude that follows an $n = 1$ profile until most of the analyte is reduced and cannot return to the oxidized state due to the kinetic limitations. The ability of mediators to support the reverse transition is limited by mass transfer and/or the bimolecular reaction and, therefore, is not accelerated at increasing E_a . In contrast, model [2] always provides a pathway to return the sample to the oxidized state. In the absence of FCN this oxidation process is accomplished via isomerization of the protein into the low potential form, which can be effectively oxidized by MG and TA. The direct and isomerization pathways are mixed using [2], yielding a broad NPSV profile with an apparent $n > 1$. The relative contributions of the two pathways depend on E_a so that the overall NPSV amplitude continuously increases with increasing E_a in contrast to a distinctive pseudo-equilibrium region using [1]. The low overall amplitudes of the $\phi_{\text{Rd}}^{\text{TauD}}$ and $\phi_{\text{Ox}}^{\text{TauD}}$ profiles in the absence of FCN provide the final argument in support of model [2]. Model [1] predicts a

contradiction between $E_{1/2}^{\text{TauD}} > 80$ mV, required to reproduce the $\phi_{\text{Rd}}^{\text{TauD}}$ amplitudes without FCN (Fig. S8), and the $E_{1/2}^{\text{TauD}} \approx 60$ mV, required to reproduce an artificial hysteresis with FCN (Figs. 4 and S6). Considering all the experimental conditions examined here, we conclude that the observed redox hysteresis arises mostly from an intrinsic redox-linked isomerization of TauD per model [2], although kinetic limitations may contribute to the observed NPSV response.

Some redox-linked reorganization of the active site is expected due to electrostatic and electronic effects on the coordinated ligands. Distinct structural conformations of metal ligands in reduced and oxidized states lead to changes in $E_{1/2}$.^{38–43} The magnitude of such changes in TauD greatly exceeds those of other currently known examples with values of < 100 mV.⁴⁴ The hysteresis of ≈ 300 mV (Table S1) is equivalent to a reversible reorganization with $\Delta G > 7$ kcal/mol ($n = 1$) or $\text{p}K_{\text{a}} > 5$, if coupled to a single protonation event ($n_{\text{H}^+} = n_{\text{e}^-}$). This observation raises an intriguing question of the extent to which ligand conformation contributes to the unusually low $\text{p}K_{\text{a}}$ of the ferric (hydr)oxo F3 species of TauD, detected by transient Raman spectroscopy.^{3,8} An uncompensated change in the $E_{1/2}$ of 7 kcal/mole would represent a substantial stabilization of TauD following the redox transition. Considering the magnitude this electrochemical relaxation and the likelihood of redox-linked protonations, it is possible that the observed decrease in $\Delta G_{\text{e}^-}^{\circ}$ is partially compensated by an increase in $\Delta G_{\text{H}^+}^{\circ}$, resulting in a small $\Delta G_{\text{tot}}^{\circ}$ in the context of the Bordwell relationship (Fig. 1). This possibility can be examined experimentally from the pH-dependence of the $E_{1/2}$ and associated vibrational changes, which is currently under investigation. The $E_{1/2}$ of the ferrous isomer of TauD reported here is over 0.5 V higher than the $\text{Fe}^{2+/3+}$ transition in CYP450.⁴⁵ If this isomer conformation is transiently retained during the catalytic cycle, the F3/F4 transition in TauD may also have a much higher $E_{1/2}$ than that of Cmp I/II of CYP450 while the $\text{p}K_{\text{a}}$ of F3 is lower than that of Cmp II. In this case, the ferrous isomer conformation would promote deprotonation of F3 that favors the alkoxide pathway in TauD over the hydroxyl radical rebinding pathway, as found in CYP450. The structural rearrangements may lead to a reduction in the oxidation potential of F4 as a protection mechanism against long-range oxidation if the reaction occurs in the absence of taurine.

The magnitude of the redox hysteresis in TauD suggests that the redox-linked reorganization involves at least one of the metal ligands: His99, Asp101, and His255 (Fig. 9a). The redox-difference vibrational changes of the amide mode (Fig. 2) suggest that structural

changes propagate beyond the first coordination shell. The redox-linked changes in protonatable residues, particularly deprotonation of histidine(s) upon oxidation, can maintain charge neutrality in the active site (a redox Bohr effect) and alter the hydrogen bonding network.⁴⁶ Initial deprotonations in TauD are likely to occur much faster than can be probed by NPSV due to accessibility of the active site for water molecules.⁴⁷ A 2.6 Å distance between N1 of His99 and the peptide carbonyl oxygen of Asn97 suggest fairly strong interactions in Fe(II)-TauD.

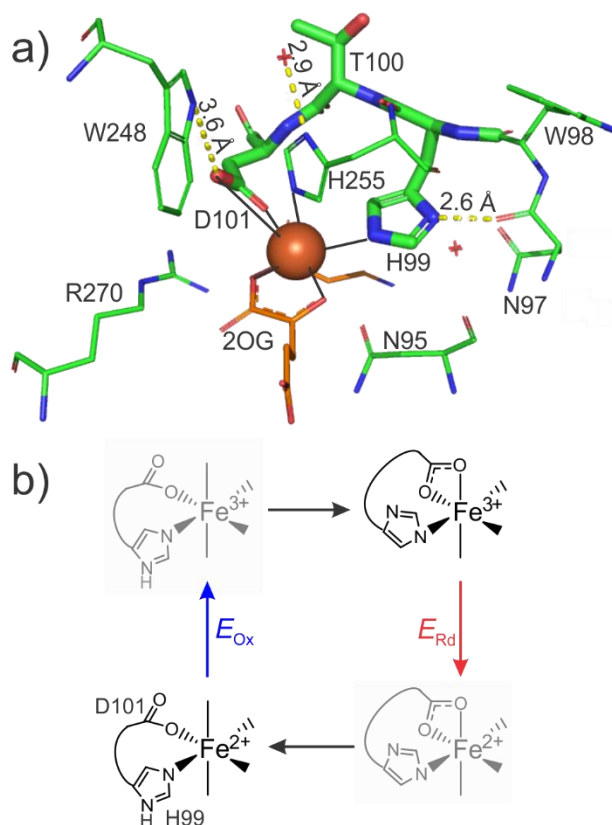


Figure 9. TauD active site structure and possible structural rearrangement. a) Selected residues at the TauD active site. The carbon atoms of 2OG and taurine are shown in orange. The peptide segment proposed to be linked to structural rearrangement is highlighted by use of stick mode. Selected hydrogen bonding interactions (yellow) and water molecules (red) are shown.⁴⁷ b) Proposed reversible redox-linked structural rearrangement.

Deprotonation of His99 upon oxidation would disrupt this interaction, allowing the Asn97-Asp101 peptide backbone to undergo further changes. This perturbation could disrupt weak interactions between Asp101 and Trp248 (3.6 Å) in Fe(II)-TauD, allowing bidentate carboxylate binding of Asp101 upon oxidation (Fig. 9b), which has been observed in other non-heme iron enzymes.⁴⁸ Such a change involving Asp101 is likely to cause a larger backbone reorganization than the initial deprotonation of histidine residue(s), but it may not be the primary trigger since Asp101 is already deprotonated in Fe(II)-TauD. The interaction of His255 with water 521 also

may be involved. Changes in both the carboxyl and imidazole moieties are consistent with redox-difference NPSV spectra of TauD. Vibrational effects of cosubstrate binding suggest that neither metal-bound water molecule(s) nor 2OG directly control isomerization, although both are affected by it. A detailed analysis of the structural origin for the redox-linked switching and its role in catalysis is currently under investigation.

CONCLUSIONS

Our results reveal extensive, fully reversible redox-linked conformational changes in three forms of TauD. The hysteresis between the oxidation and reduction Nernstian NPSV profiles arises primarily from isomerization between two separate ferric/ferrous redox couples of the protein. Quantitative kinetic modeling shows that a redox-linked conformational switching process substantially improves the fitness of simulations compared to the experimental data across various conditions over a simple model with a single redox potential. Changes in the redox potential of up to 0.3 V are attributed to the reversible reorganization of the metal center primary ligands, leading to further reorganization of the protein backbone.

Acknowledgements

This work was supported by the National Institutes of Health grants GM096132 and GM063584.

Supporting Information:

Detailed method for NPSV potential profile; NPSV data for Fe-TauD, 2OG-Fe-TauD, and taurine-2OG-Fe-TauD and a table detailing observed $E_{1/2}$ of each complex; NPSV of Zn bound 2OG-TauD; Tables detailing thermodynamic and kinetic properties of mediators; Diagrams of chemical models; Experimental data used to estimate rate of conformational change; Expanded set of simulations and tables detailing results.

REFERENCES

- (1) Herr, C. Q.; Hausinger, R. P. Amazing Diversity in Biochemical Roles of Fe(II)/2-Oxoglutarate Oxygenases. *Trends Biochem. Sci.* **2018**, *43*, 517–532. <https://doi.org/10.1016/j.tibs.2018.04.002>.
- (2) Lewis, J. C.; Coelho, P. S.; Arnold, F. H. Enzymatic Functionalization of Carbon-Hydrogen Bonds. *Chem. Soc. Rev.* **2011**, *40*, 2003–2021. <https://doi.org/10.1039/c0cs00067a>.
- (3) Proshlyakov, D. A.; Hausinger, R. P. Transient Iron Species in the Catalytic Mechanism of the Archetypal α -Ketoglutarate-Dependent Dioxygenase, TauD. In *Iron-Containing Enzymes: Versatile Catalysts of Hydroxylation Reactions in Nature*; Visser, S. P. De, Kumar, D., Eds.; Royal Society of Chemistry, 2012; pp 67–87.
- (4) Proshlyakov, D. A.; McCracken, J.; Hausinger, R. P. Spectroscopic Analyses of 2-Oxoglutarate-Dependent Oxygenases: TauD as a Case Study. *J. Biol. Inorg. Chem.* **2017**, *22*, 367–379. <https://doi.org/10.1007/s00775-016-1406-3>.
- (5) Eichhorn, E.; Van Der Ploeg, J. R.; Kertesz, M. A.; Leisinger, T. Characterization of α -Ketoglutarate-Dependent Taurine Dioxygenase from *Escherichia coli*. *J. Biol. Chem.* **1997**, *272*, 23031–23036. <https://doi.org/10.1074/jbc.272.37.23031>.
- (6) Price, J. C.; Barr, E. W.; Glass, T. E.; Krebs, C.; Bollinger, J. M. Evidence for Hydrogen Abstraction from C1 of Taurine by the High-Spin Fe(IV) Intermediate Detected during Oxygen Activation by Taurine: α -Ketoglutarate Dioxygenase (TauD). *J. Am. Chem. Soc.* **2003**, *125*, 13008–13009. <https://doi.org/10.1021/ja037400h>.
- (7) Martinez, S.; Hausinger, R. P. Catalytic Mechanisms of Fe(II)- and 2-Oxoglutarate-Dependent Oxygenases. *J. Biol. Chem.* **2015**, *290*, 20702–20711. <https://doi.org/10.1074/jbc.R115.648691>.
- (8) Grzyska, P. K.; Appelman, E. H.; Hausinger, R. P.; Proshlyakov, D. A. Insight into the Mechanism of an Iron Dioxygenase by Resolution of Steps Following the FeIV=O Species. *Proc. Natl. Acad. Sci. U. S. A.* **2010**, *107*, 3982–3987. <https://doi.org/10.1073/pnas.0911565107>.
- (9) Poulos, T. L. Heme Enzyme Structure and Function. *Chem. Rev.* **2014**, *114*, 3919–3962. <https://doi.org/10.1021/cr400415k>.
- (10) Mitchell, A. J.; Dunham, N. P.; Martinie, R. J.; Bergman, J. A.; Pollock, C. J.; Hu, K.; Allen, B. D.; Chang, W.; Silakov, A.; Bollinger, J. M.; et al. Visualizing the Reaction Cycle in an Iron(II)- and 2-(Oxo)-Glutarate-Dependent Hydroxylase. *J. Am. Chem. Soc.* **2017**, *139*, 13830–13836. <https://doi.org/10.1021/jacs.7b07374>.
- (11) Gupta, R.; Borovik, A. S. Monomeric Mn^{III/II} and Fe^{III/II} Complexes with Terminal Hydroxo and Oxo Ligands : Probing Reactivity via O - H Bond Dissociation Energies. *J. Am. Chem. Soc.* **2003**, *125*, 13234–13242.
- (12) Li, L.; Li, C.; Zhang, Z.; Alexov, E. On the Dielectric “Constant” of Proteins: Smooth Dielectric

- Function for Macromolecular Modeling and Its Implementation in DelPhi. *J. Chem. Theory Comput.* **2013**, 9 (4), 2126–2136. <https://doi.org/10.1021/ct400065j>.
- (13) Bordwell, F. G.; Ji, G. Z.; Satish, A. V.; Zhang, X.; Cheng, J. P. Bond Dissociation Energies in DMSO Related to the Gas Phase. *J. Am. Chem. Soc.* **1991**, 113, 9790–9795. <https://doi.org/10.1021/ja00026a012>.
 - (14) Mayer, J. M. Hydrogen Atom Abstraction by Metal-Oxo Complexes: Understanding the Analogy with Organic Radical Reactions. *Acc. Chem. Res.* **1998**, 31, 441–450. <https://doi.org/10.1021/ar970171h>.
 - (15) Yosca, T. H.; Rittle, J.; Krest, C. M.; Onderko, E. L.; Silakov, A.; Calixto, J. C.; Behan, R. K.; Green, M. T. Iron(IV)Hydroxide pK_a and the Role of Thiolate Ligation in C-H Bond Activation by Cytochrome P450. *Science* **2013**, 342, 825–829. <https://doi.org/10.1126/science.1244373>.
 - (16) Green, M. T.; Park, U. V; Pennsylv, V. Application of Badger's Rule to Heme and Non-Heme Iron - Oxygen Bonds : An Examination of Ferryl Protonation States Depends on the One-Electron Reduction Potential of Compound I. *J. Am. Chem. Soc.* **2006**, 128, 1902–1906.
 - (17) Sitter, A. J.; Reczek, C. M.; Terners, J. Heme-Linked Ionization of Horseradish Peroxidase Compound II Monitored by the Resonance Raman Fe(IV)=O Stretching Vibration. *J. Biol. Chem.* **1985**, 260, 7515–7522.
 - (18) Brischwein, M.; Scharf, B.; Engelhard, M.; Mäntele, W. Analysis of the Redox Reaction of an Archaeobacterial Copper Protein, Halocyanin, by Electrochemistry and FTIR Difference Spectroscopy. *Biochemistry* **1993**, 32, 13710–13717. <https://doi.org/10.1021/bi00212a041>.
 - (19) Hirst, J. Elucidating the Mechanisms of Coupled Electron Transfer and Catalytic Reactions by Protein Film Voltammetry. *Biochim. Biophys. Acta - Bioenerg.* **2006**, 1757, 225–239. <https://doi.org/10.1016/j.bbabbio.2006.04.002>.
 - (20) Grzyska, P. K.; Hausinger, R. P.; Proshlyakov, D. A. Metal and Substrate Binding to an Fe(II) Dioxygenase Resolved by UV Spectroscopy with Global Regression Analysis. *Anal. Biochem.* **2010**, 399, 64–71. <https://doi.org/10.1016/j.ab.2009.11.022>.
 - (21) Moss, D.; Nabedryk, E.; Breton, J.; Mäntele, W. Redox-linked Conformational Changes in Proteins Detected by a Combination of Infrared Spectroscopy and Protein Electrochemistry: Evaluation of the Technique with Cytochrome C. *Eur. J. Biochem.* **1990**, 187, 565–572. <https://doi.org/10.1111/j.1432-1033.1990.tb15338.x>.
 - (22) Moss, D. A.; Leonhard, M.; Bauscher, M.; Mäntele, W. Electrochemical Redox Titration of Cofactors in the Reaction Center from *Rhodobacter sphaeroides*. *FEBS Lett.* **1991**, 283, 33–36.
 - (23) Fritz, F.; Moss, D. A.; Mäntele, W. Electrochemical Titration of the Cytochrome Hemes in the *Rhodopseudomonas viridis* Reaction Center Cyclic Equilibrium Titrations Yield Midpoint

- Potentials without Evidence for Heme Cooperativity. *FEBS Lett.* **1992**, 297, 167–170.
[https://doi.org/10.1016/0014-5793\(92\)80352-H](https://doi.org/10.1016/0014-5793(92)80352-H).
- (24) Clair, C. S. S.; Gray, H. B.; Valentine, J. S. Spectroelectrochemistry of Copper-Zinc Superoxide Dismutase. *Inorg. Chem.* **1992**, 31, 925–927. <https://doi.org/10.1021/ic00031a041>.
 - (25) DeLacey, A. L.; Stadler, C.; Fernandez, V. M.; Hatchikian, E. C.; Fan, H. J.; Li, S.; Hall, M. B. IR Spectroelectrochemical Study of the Binding of Carbon Monoxide to the Active Site of *Desulfovibrio fructosovorans* Ni-Fe Hydrogenase. *J. Biol. Inorg. Chem.* **2002**, 7, 318–326.
<https://doi.org/10.1007/s00775-001-0301-7>.
 - (26) DeLacey, A. L.; Fernandez, V. M.; Rousset, M.; Cavazza, C.; Hatchikian, E. C. Spectroscopic and Kinetic Characterization of Active Site Mutants of *Desulfovibrio fructosovorans* Ni-Fe Hydrogenase. *J. Biol. Inorg. Chem.* **2003**, 8, 129–134. <https://doi.org/10.1007/s00775-002-0397-4>.
 - (27) Mantele, W. Reaction-Induced Infrared Difference Spectroscopy for the Study of Protein Function and Reaction Mechanisms. *Trends Biochem. Sci.* **1993**, 18, 197–202.
 - (28) Vincent, K. A. Triggered Infrared Spectroscopy for Investigating Metalloprotein Chemistry. *Philos. Trans. A. Math. Phys. Eng. Sci.* **2010**, 368, 3713–3731.
<https://doi.org/10.1098/rsta.2010.0055>.
 - (29) Melin, F.; Hellwig, P. Recent Advances in the Electrochemistry and Spectroelectrochemistry of Membrane Proteins. *Biol. Chem.* **2013**, 394, 593–609. <https://doi.org/10.1515/hsz-2012-0344>.
 - (30) Ash, P. A.; Vincent, K. A. Spectroscopic Analysis of Immobilised Redox Enzymes under Direct Electrochemical Control. *Chem. Commun.* **2012**, 48, 1400–1409.
<https://doi.org/10.1039/C1CC15871F>.
 - (31) John, C. W.; Proshlyakov, D. A. FTIR Spectro-Voltammetry and Quantitative Modeling of Analytes in Kinetically Constrained Redox Mixtures. *Anal. Chem.* **2019**, xx, xx–xx.
<https://doi.org/10.1021/acs.analchem.9b00859>
 - (32) Ryle, M. J.; Padmakumar, R.; Hausinger, R. P. Stopped-Flow Kinetic Analysis of *Escherichia coli* Taurine/ α -Ketoglutarate Dioxygenase: Interactions with α -Ketoglutarate, Taurine, and Oxygen. *Biochemistry* **1999**, 38, 15278–15286. <https://doi.org/bi9912746> [pii].
 - (33) Yao, C.; Capdevielle, F. J.; Kadish, K. M.; Bear, J. L. Thin-Layer Microcell for Transmittance Fourier Transform Infrared Spectroelectrochemistry. *Anal. Chem.* **1989**, 61, 2805–2809.
 - (34) Arciero, D. M.; Hooper, A. B.; Collins, M. J. Preliminary Note Low Volume Spectroelectrochemistry : An Anaerobic Optically Transparent Thin Layer Electrode Cell and a Potentiostat 1 UV-Vis Spectrophotometer Interface for Computer-Controlled Data Collection. *J. Electroanal. Chem.* **1994**, 371, 277–281.
 - (35) <https://github.com/dap-biospec/G3F>.

- (36) <https://github.com/dap-biospec/KinESim>.
- (37) Susi, H. Infrared Spectra and Protein in Aqueous Solutions. *J. Biol. Chem.* **1967**, *242*, 5460–5467.
- (38) Costentin, C. Electrochemical Approach to the Mechanistic Study of Proton-Coupled Electron Transfer. *Chem. Rev.* **2008**, *108*, 2145–2179. <https://doi.org/10.1021/cr068065t>.
- (39) Murgida, D. H.; Hildebrandt, P. Redox and Redox-Coupled Processes of Heme Proteins and Enzymes at Electrochemical Interfaces. *Phys. Chem. Chem. Phys.* **2005**, *7*, 3773–3784. <https://doi.org/10.1039/b507989f>.
- (40) Armstrong, F. A.; Camba, R.; Heering, H. A.; Hirst, J.; Jeuken, L. J.; Jones, A. K.; Léger, C.; McEvoy, J. P. Fast Voltammetric Studies of the Kinetics and Energetics of Coupled Electron-Transfer Reactions in Proteins. *Faraday Discuss.* **2000**, *116*, 191–203; discussion 257–268. <https://doi.org/10.1039/b002290j>.
- (41) Léger, C.; Bertrand, P. Direct Electrochemistry of Redox Enzymes as a Tool for Mechanistic Studies Direct Electrochemistry of Redox Enzymes as a Tool for Mechanistic Studies. *Chem. Rev.* **2008**, *108*, 2379–2438. <https://doi.org/10.1021/cr0680742>.
- (42) Jeuken, L. J. C.; Armstrong, F. A. Electrochemical Origin of Hysteresis in the Electron-Transfer Reactions of Adsorbed Proteins: Contrasting Behavior of the “Blue” Copper Protein, Azurin, Adsorbed on Pyrolytic Graphite and Modified Gold Electrodes. *J. Phys. Chem. B* **2001**, *105*, 5271–5282. <https://doi.org/10.1021/jp004283t>.
- (43) Pulcu, G. S.; Elmore, B. L.; Arciero, D. M.; Hooper, A. B.; Elliott, S. J. Direct Electrochemistry of Tetraheme Cytochrome C₅₅₄ from *Nitrosomonas europaea*: Redox Cooperativity and Gating. *J. Am. Chem. Soc.* **2007**, *129*, 1838–1839. <https://doi.org/10.1021/ja065657k>.
- (44) Hosseinzadeh, P.; Lu, Y. Design and Fine-Tuning Redox Potentials of Metalloproteins Involved in Electron Transfer in Bioenergetics. *Biochim. Biophys. Acta - Bioenerg.* **2016**, *1857*, 557–581. <https://doi.org/10.1016/j.bbabo.2015.08.006>.
- (45) Mittra, K.; Green, M. T. Reduction Potentials of P450 Compounds I and II: Insight into the Thermodynamics of C-H Bond Activation. *J. Am. Chem. Soc.* **2019**, *141* (13), 5504–5510. <https://doi.org/10.1021/jacs.9b00242>.
- (46) Papa, S. Proton Translocation Reactions in the Respiratory Chains. *Biochim. Biophys. Acta* **1976**, *456*, 39–84. [https://doi.org/10.1016/0304-4173\(76\)90008-2](https://doi.org/10.1016/0304-4173(76)90008-2).
- (47) Elkins, J. M.; Ryle, M. J.; Clifton, I. J.; Hotopp, J. C. D.; Lloyd, J. S.; Burzlaff, N. I.; Baldwin, J. E.; Hausinger, R. P.; Roach, P. L. X-Ray Crystal Structure of *Escherichia coli* Taurine/α-Ketoglutarate Dioxygenase Complexed to Ferrous Iron and Substrates. *Biochemistry* **2002**, *41*, 5185–5192.
- (48) Karlsson, A.; Parales, J. V.; Parales, R. E.; Gibson, D. T.; Eklund, H.; Ramaswamy, S. Crystal

Structure of Naphthalene Dioxygenase : Side-on Binding of Dioxygen to Iron. *Science* (80-.).
2003, 299, 1039–1043.

**Strongly coupled redox-linked conformational switching at the active site of
the non-heme iron-dependent dioxygenase, TauD**

Christopher W. John,¹ Greg M. Swain,¹ Robert P. Hausinger,^{2,3} and Denis A. Proshlyakov¹

1 Department of Chemistry, Michigan State University, East Lansing, MI 48824, USA

2 Department of Microbiology and Molecular Genetics, Michigan State University,
East Lansing, MI 48824, USA

3 Department of Biochemistry and Molecular Biology, Michigan State University, East
Lansing, MI 48824, USA

Table of Contents

Figure S1 Potential profile of NPSV	S2
Figure S2 Deconvolution of NPSV FTIR data	S2
Figure S3 NPSV/GSR resolution of redox transitions in Fe-TauD, 2OG-Fe-TauD, and taurine-2OG-Fe-TauD	S3
Figure S4 NPSV/GSR resolution of redox transitions in 2OG-TauD with Zn or Fe bound	S3
Table S1 Reduction and oxidation potentials of TauD calculated from experimental NPSV profiles	S4
Table S2 List of mediators used during NPSV and their thermodynamic and kinetic properties.....	S4
Table S3 Complete list of mediators tested for NPSV of TauD.....	S4
Figure S5 Graphical representation of the reduced quantitative model.	S5
Figure S6 Titration of 2OG-Fe(II)-TauD into FCN.....	S5
Figure S7 Extended simulations showing the effect of thermodynamic properties of the analyte on the apparent NPSV redox hysteresis	S6
Table S4 Calculated oxidation and reduction potentials of profiles generated using model [1].....	S7
Figure S8 Effect of thermodynamic properties of the analyte on the apparent NPSV redox hysteresis when FCN is not present	S8

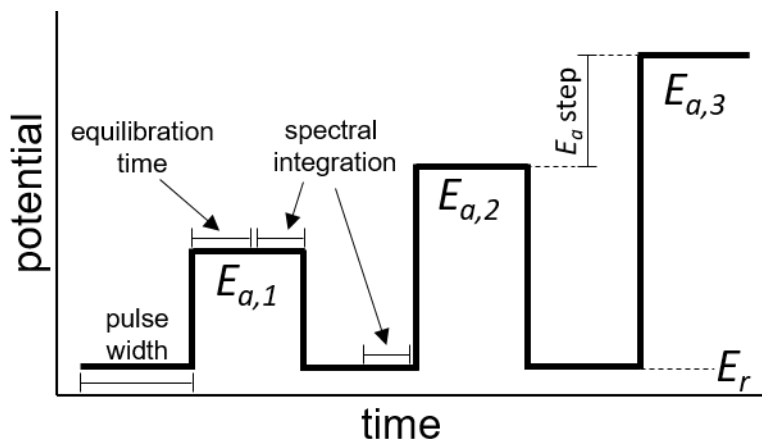


Figure S1. Illustration of the time-dependent profile of potentials used during NPSV. E_a alternates between a constant reference, E_r , and a variable applied potential, $E_{a,i}$, over successive cycles.

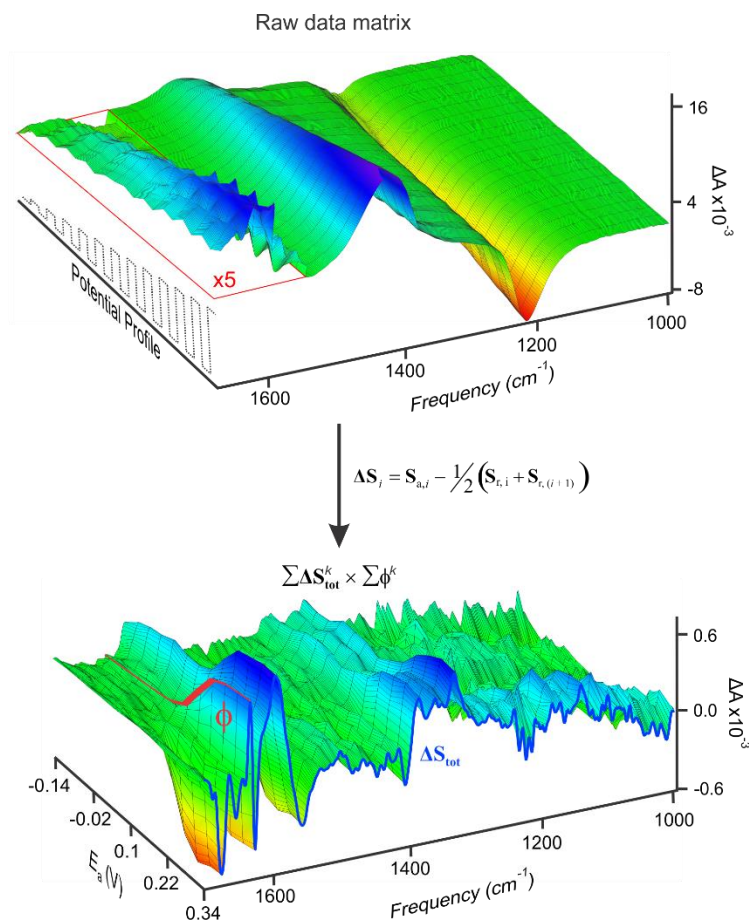


Figure S2. Deconvolution of NPSV FTIR data. Equation (1) was used to process a raw FTIR data (top) into a redox-difference spectral matrix (bottom), which was contributed by all components (k), including redox mediators. These data were further deconvoluted into ΔS_{tot} spectra and ϕ profiles of individual components, as shown for TauD by the superimposed blue and red traces, respectively.

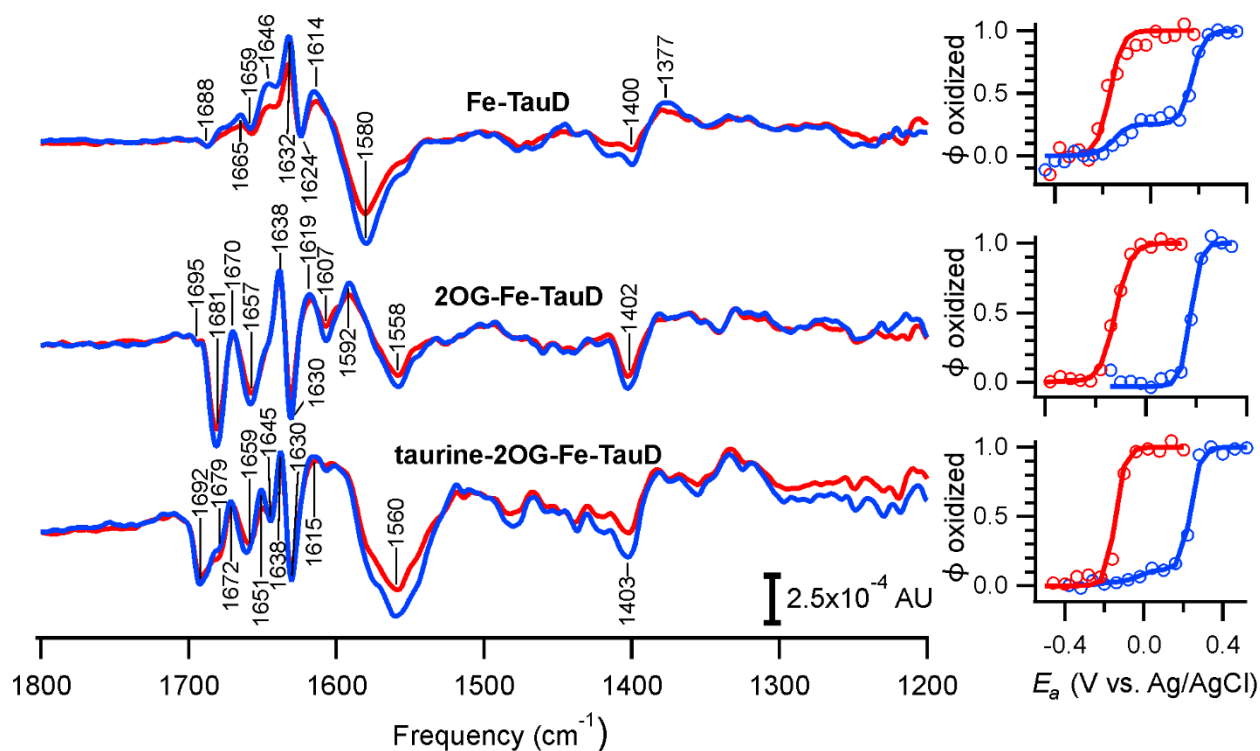


Figure S3. NPSV/GSR resolution of redox transitions in Fe-TauD, 2OG-Fe-TauD, and taurine-2OG-Fe-TauD. Samples were measured in 25 mM Tris, pH 8.5, containing 0.5 M KCl. A mediator cocktail consisting of 100 μ M MG, 100 μ M TA, and 100 μ M FCN was present in all samples. **Left:** ΔS_{tot} of the reduction (—) and oxidation (—) steps. Positive modes represent ferric TauD and negative modes represent ferrous TauD. **Right:** Experimental profiles of reduction steps (○) and oxidation steps (○), normalized using $\Delta A_{1632}^{Fe-TauD}$, $\Delta A_{1681}^{2OG-Fe-TauD}$, and $\Delta A_{1692}^{taurine-2OG-Fe-TauD}$, and the fitted ϕ profiles (—, —).

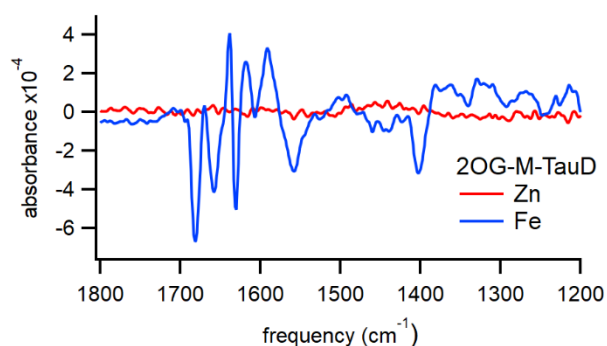


Figure S4. NPSV/GSR resolution of redox transitions when comparing 2OG-TauD with Zn or Fe bound. Both samples were prepared in 25 mM Tris, pH 8.5, containing 0.5 M KCl and a mediator cocktail consisting of 100 μ M each of MG, TA, and FCN.

Table S1. Reduction and oxidation potentials of TauD calculated from experimental NPSV profiles. The maximal magnitude of the observed hysteresis ($\Delta E_{1/2}$) is shown.

TauD forms	E_{Rd} (mV)	E_{Ox} (mV)		$\Delta E_{1/2}$ (mV)
		Phase 1	Phase 2	
Fe-TauD	-154 ± 22	-153 ± 20	187 ± 19	341
2OG-Fe-TauD	-127 ± 21	-	171 ± 17	298
Taurine-2OG-Fe-TauD	-124 ± 16	-134 ± 48	174 ± 48	298

Table S2. List of mediators used during NPSV measurements with their thermodynamic and kinetic properties. $E_{1/2}$ is measured versus a Ag/AgCl reference, n is the electron transfer coefficient, k_{el}^* and k_{lim} are defined separately^a, and k_{sol} is a homogeneous bimolecular rate constant for the reaction with TauD. All values were determined empirically.

Mediator	$E_{1/2}$ (mV)	n	k_{el}^* (s ⁻¹)	k_{lim} (s ⁻¹)	k_{sol} (M ⁻¹ s ⁻¹)
FCN	215 ^b	1	0.1	0.2	2.0×10^4
MG	-111, -243	1, 1	0.025	0.5	1.4×10^4
TA	-197 ^c	2	0.5	1.88	1.7×10^4

^a John, C. W.; Proshlyakov, D. A. *Anal. Chem.* **2019**, xx, xx–xx.

^b Kolthoff, I. M.; Tomsicek, W. J. *J. Phys. Chem.* **1934**, 39 (7), 945

^c Chen, H. Y.; Zhou, D. M.; Xu, J. J.; Fang, H. Q. *J. Electroanal. Chem.* **1997**, 422 (1–2), 21

Table S3. Complete list of mediators tested for NPSV of TauD.

Mediator	$E_{1/2}$ (mV)	n
FCN ^a	215	1
Ru(NH ₃) ₆ ^b	100	1
2,3,5,6-TMPD ^{c,d}	52	1
N,N,N',N'-TMPD ^{c,d}	25	1
indophenol ^c	-9	2
1,2-naphthoquinone ^c	-42	2
Fe-EDTA ^c	-82	1
MG	-111, -243	1, 1
TA ^c	-197	2
methylene blue ^c	-236	2
methyl viologen ^c	-687	2

^a Kolthoff, I. M.; Tomsicek, W. J. *J. Phys. Chem.* **1934**, 39 (7), 945

^b Meyer, T. J.; Taube, H. *Inorg. Chem.* **1968**, 7 (11), 2369

^c Fultz, M. Lou; Durst, R. A. *Anal. Chim. Acta* **1982**, 140 (1), 1

^d Rawson, F. J.; Downard, A. J.; Baronian, K. H. *Sci. Rep.* **2015**, 4 (1), 5216

^e Chen, H. Y.; Zhou, D. M.; Xu, J. J.; Fang, H. Q. *J. Electroanal. Chem.* **1997**, 422 (1–2), 21

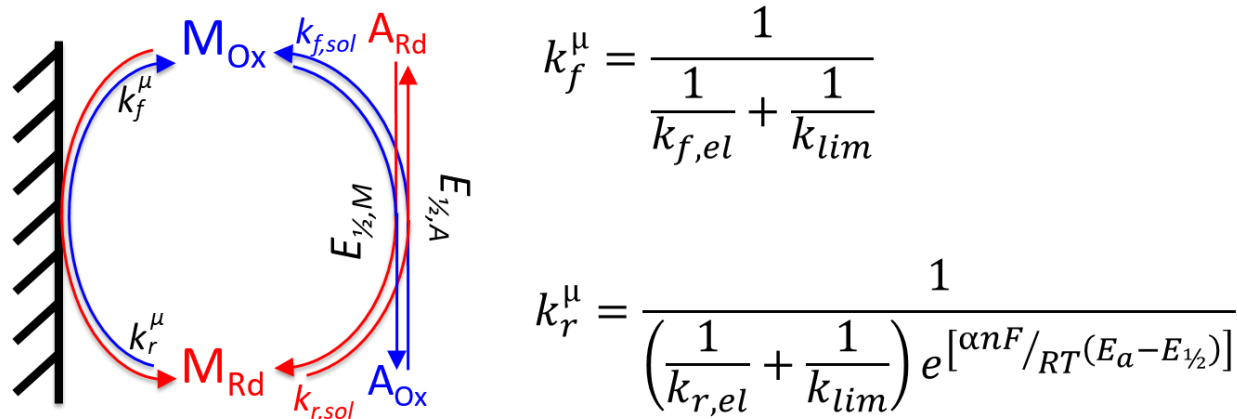


Figure S5. Graphical representation of the reduced quantitative model. M represents the mediator that facilitates electron transfer between the electrode and an analyte, A. The model reduces the electron transfer process of the mediator with the electrode using a reduced rate constant (k_f^μ , k_r^μ) that considers both the rate constant of the electron transfer and mass transfer on and off of the electrode¹. The model also considers the electron transfer between the mediators and analyte ($k_{f,sol}$, $k_{r,sol}$), the applied potential at the electrode surface (E_{app}), and $E_{1/2}$ of each component.

¹John, C. W.; Proshlyakov, D. A. FTIR Spectro-Voltammetry and Quantitative Modeling of Analytes in Kinetically Constrained Redox Mixtures. *Anal. Chem.* **2019**, xx, xx–xx.

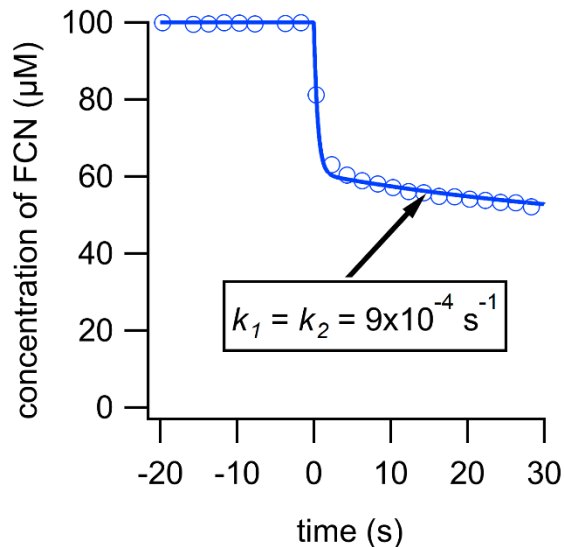


Figure S6. Titration of 70 μM 2OG-Fe(II)-TauD into 100 μM FCN. The initial electron transfer rate between TauD and FCN was calculated to be $\gg 15,000 \text{ M}^{-1}\text{s}^{-1}$. The value of k_2 , the conversion rate in model [2], is estimated to be $9 \times 10^{-4} \text{ s}^{-1}$ based on the rate of the continued reduction of FCN beginning at about 5 s.

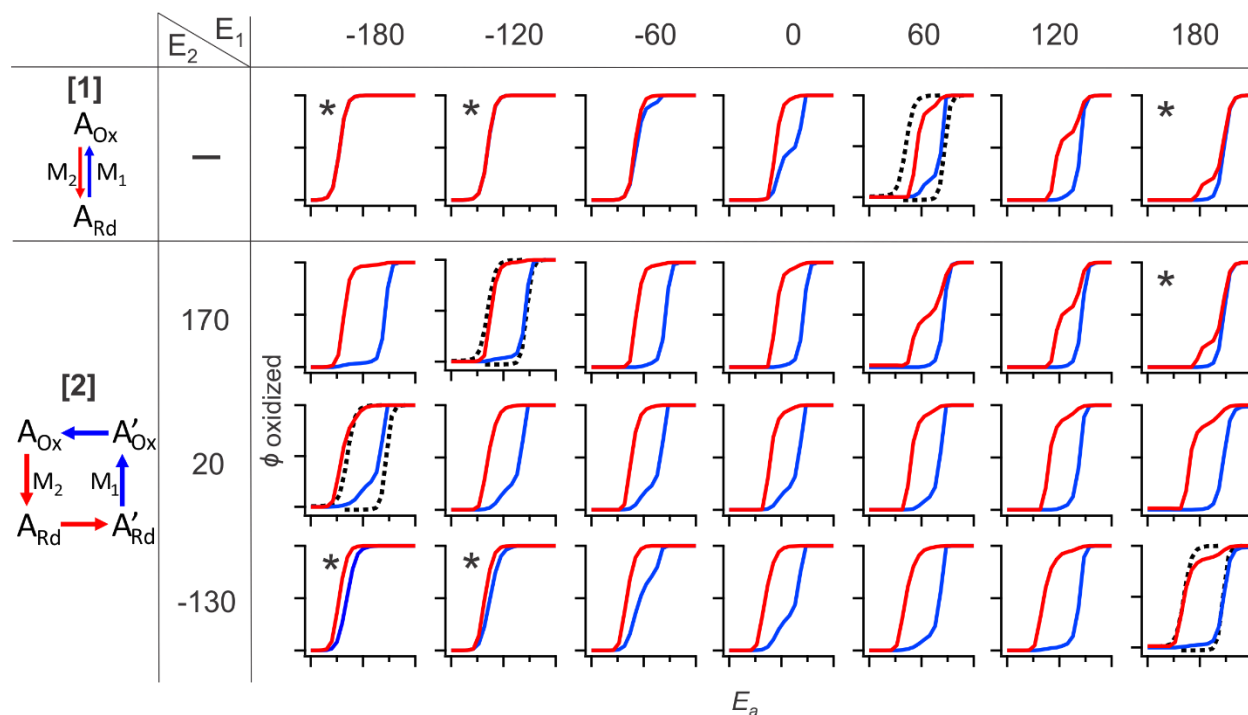


Figure S7. Extended simulations showing the effect of the thermodynamic properties of the analyte on the apparent NPSV redox hysteresis. Population profiles ϕ_{Rd}^A (red) and ϕ_{Ox}^A (blue) were simulated using models **[1]** (top) and **[2]** (bottom). Simulations were carried out for a 1 mM analyte using the actual experimental conditions and empirical mediator parameters. The $E_{1/2}$ values of the analyte are shown by E_1 (for model **[1]**) or E_1 and E_2 (for model **[2]**) in mV. Full scales are $-0.4 \text{ V} \leq E_a \leq +0.4 \text{ V}$ and $0 \text{ mM} \leq C_{Ox} \leq 1 \text{ mM}$ for x and y axes, respectively, for all plots. Population profiles of **[2]** are the sum of both conformations. Conditions that exhibit predominantly Nernstian behavior are indicated by *. Dashed lines show experimental NPSV profiles of 2OG-Fe-TauD as a reference for selected simulated conditions with comparable levels of hysteresis ($\Delta E_{1/2} = 298 \pm 27 \text{ mV}$).

Table S4. Calculated oxidation and reduction potentials of profiles generated using model [1]. Phases representing >50% of the observed oxidation or reduction are bolded. The largest observed hysteresis is italicized.

$E_{1/2}$ actual (mV)	E_{Ox1} (mV)	E_{Ox2} (mV)	E_{Rd1} (mV)	E_{Rd2} (mV)	$\Delta E_{1/2,max}$ (mV)	$\Delta E_{1/2,major}$ (mV)
200		200	201	16.7	183	1
180		180	187	-15	195	7
160		160	174	-19.5	180	14
140	126	169	162	-27.8	197	7
120	101	164	151	-33.2	197	197
100	59.5	160	139	-37.4	197	197
80	38.2	158	127	-40.5	199	199
60	18.9	156	114	-42.6	199	199
40	3.55	155	88.7	-45.1	200	200
20	-10.1	153	41.9	-49.1	202	202
0	-22.6	151	<i>-10.4</i>	-62	<i>213</i>	<i>213</i>
-20	-35	146	-17.3	-65.6	212	30.6
-40	-47.6	130	-17.7	-70.3	200	22.7
-60	-61.3	113	-2.02	-74.6	188	13.3
-80	-78.7	113		-83.6	197	4.9
-100	-99.0			-102	3	3
-120	-120			-120	0	0
-140	-140			-140	0	0
-160	-160			-160	0	0
-180	-180			-180	0	0
-200	-200			-200	0	0

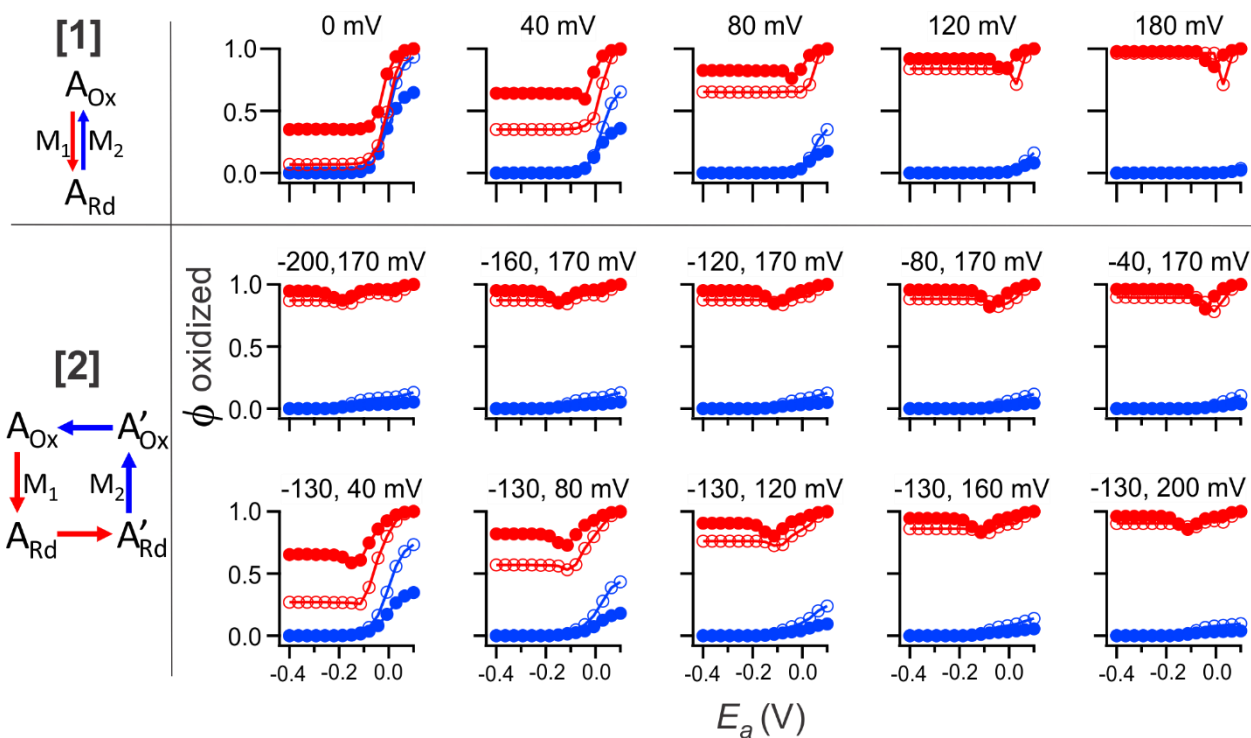


Figure S8. Effect of thermodynamic properties of the analyte on the apparent NPSV redox hysteresis when FCN is not present. Simulations were carried out for 1 mM analyte in the presence of 0.5 mM MG and TA. The $E_{1/2}$ of the analyte is indicated above each simulation set for model [1] and both values are shown for model [2]. Population profiles using model [2] are the sum of both conformations A and A'. Simulations were carried out using a 300 s pulse width (closed circles) and 1000 s pulse width (open circles).